




Proposal for a hybrid clock system consisting of passive and active optical clocks and a fully stabilized microcomb

DESHUI YU,^{1,*}  FRANK VOLLMER,^{2,6} PASCAL DEL'HAYE,^{3,4,7} AND SHOUGANG ZHANG^{1,5,8}

¹National Time Service Center, Chinese Academy of Sciences, Xi'an 710600, China

²Physics and Astronomy, University of Exeter, Exeter EX4 4QD, United Kingdom

³Max Planck Institute for the Science of Light, 91058 Erlangen, Germany

⁴Department of Physics, Friedrich Alexander University Erlangen Nuremberg, 91058 Erlangen, Germany

⁵University of Chinese Academy of Sciences, Beijing 100049, China

⁶f.vollmer@exeter.ac.uk

⁷pascal.delhaye@mpl.mpg.de

⁸szhang@ntsc.ac.cn

*deshuiyu@ntsc.ac.cn

Abstract: Optical atomic clocks produce highly stable frequency standards and frequency combs bridge clock frequencies with hundreds of terahertz difference. In this paper, we propose a hybrid clock scheme, where a light source pumps an active optical clock through a microresonator-based nonlinear third harmonic process, serves as a passive optical clock via indirectly locking its frequency to an atomic transition, and drives a chip-scale microcomb whose mode spacing is stabilized using the active optical clock. The operation of the whole hybrid system is investigated through simulation analysis. The numerical results show: (i) The short-term frequency stability of the passive optical clock follows an Allan deviation of $\sigma_y(\tau) = 9.3 \times 10^{-14} \tau^{-1/2}$ with the averaging time τ , limited by the population fluctuations of interrogated atoms. (ii) The frequency stability of the active optical clock reaches $\sigma_y(\tau) = 6.2 \times 10^{-15} \tau^{-1/2}$, which is close to the quantum noise limit. (iii) The mode spacing of the stabilized microcomb has a shot-noise-limited Allan deviation of $\sigma_y(\tau) = 1.9 \times 10^{-11} \tau^{-1/2}$. Our hybrid scheme may be realized using recently developed technologies in (micro)photonics and atomic physics, paving the way towards on-chip optical frequency comparison, synthesis, and synchronization.

Published by Optica Publishing Group under the terms of the [Creative Commons Attribution 4.0 License](https://creativecommons.org/licenses/by/4.0/). Further distribution of this work must maintain attribution to the author(s) and the published article's title, journal citation, and DOI.

1. Introduction

Metrology deals with high precision measurements of physical parameters, among which frequency can be determined with the highest degree of accuracy using atomic clocks [1,2]. Thus far, optical clocks have surpassed their microwave counterparts in both stability and accuracy by over two orders of magnitude [3–5], which paves the way towards an optical redefinition of the SI second. Most optical clocks are operated in a passive fashion, where the frequency of a pre-stabilized laser is referenced to a narrow-line optical transition of carefully engineered atoms [6]. Active optical clocks, which directly produce highly stable optical frequency standards without extra steps of stabilizing the laser frequency to an atomic transition, have also been proposed [7] and demonstrated [8]. Indeed, the underlying mechanism of such active operation is the substantial suppression of the cavity pulling effect on the lasing dynamics in the so-called bad-cavity limit. Frequency comparison is essential for evaluating the performance of an atomic clock and optical frequency combs bridge frequency standards from microwave to optical domain with orders of magnitude difference, facilitating the frequency comparison between different

atomic clocks [9]. Yet, to our best knowledge, the direct frequency comparison between passive and active optical clocks through a frequency comb has not been demonstrated.

Engineering integrated metrology systems that include optical frequency comparison, synchronization, and synthesis benefits broad out-of-the-lab applications such as satellite-based geo-positioning and communication [10]. Its implementation demands a vast simplification of the metrology configuration and the subtle design of each component, for example, reducing the numbers of light sources and optical cavities and minimizing their physical volumes. Owing to ultrahigh Q factors and small mode volumes, whispering-gallery-mode (WGM) microresonators enable nonlinear frequency conversion at low pump thresholds and large conversion efficiencies at room temperature [11–13]. In particular, microresonator-based frequency combs, i.e., microcombs, which make use of the nonlinear Kerr process and four-wave mixing, possess the advantages of miniaturized size, simple structure, and low power consumption, compared to conventional optical frequency combs. Recently, microcombs have been employed in diverse fields, including atomic and molecular spectroscopy [14], integrated photonics for optical communications and data processing [15], and chip-scale frequency metrology [16]. Various approaches of fully stabilizing microcombs have been exploited, for example, referencing two comb modes respectively to two atomic transitions through frequency doubling [17] and $f - 2f$ self-referencing in an octave-spanning spectrum [18]. Nevertheless, the microcomb spectra mainly cover the infrared regime while the wavelengths of most optical clocks are in the visible band. Extending the microcomb spectra to the visible regime is still challenging [19,20].

In this paper, we propose a hybrid clock scheme, where the full stabilization of a Kerr microcomb is implemented using two optical atomic clocks that are operated in distinct, i.e., passive and active, modes. Both clock wavelengths, 1359 and 1377 nm, are in the infrared regime that is accessible by the microcomb spectrum. The whole system contains only one light source that also serves as a passive optical clock via indirectly locking its frequency to an atomic transition. Other optical modes at different wavelengths are generated through the third harmonic (TH) nonlinear optical process and the lasing action. We evaluate the performance of optical clocks and microcomb through the simulation analysis. The numerical results show that the frequency stabilities of passive and active optical clocks follow $9.3 \times 10^{-14} \tau^{-1/2}$ and $6.2 \times 10^{-15} \tau^{-1/2}$, respectively, with the averaging time τ , and the mode spacing of the microcomb has an Allan deviation of $\sigma_y(\tau) = 1.9 \times 10^{-11} \tau^{-1/2}$. Recent technologies in (micro)photonics and atomic physics ensure the successful implement of the proposed hybrid scheme.

2. Physical system

Figure 1(a) illustrates the hybrid clock scheme, in which there is only one light source at $\lambda_{\text{clock1}} = 1377$ nm. This light source may be a commercial laser system. As we will see below, the light source can serve as a passive optical clock by indirectly locking its frequency to an atomic transition. The laser beam is split into two sub-beams. One sub-beam enters the microcavity I, where the TH optical wave at $\lambda_{\text{TH}} = 459$ nm is generated. The output TH light excites the ensemble I of ^{133}Cs atoms from the ground $|1\rangle = 6s^2S_{1/2}$ state to the excited $|4\rangle = 7p^2P_{1/2}$ state. Atoms in $|4\rangle$ emit fluorescent photons that are collected by a photodetector (PD). The electrical signal produced by the PD is fed back into the light source, indirectly stabilizing its central frequency $\omega_{\text{clock1}} = 2\pi c/\lambda_{\text{clock1}}$ to the atomic $|1\rangle - |4\rangle$ transition. Here, c is the speed of light in vacuum. Passing an optical amplifier (OA), the TH light further drives the ^{133}Cs ensemble II that is placed inside a low- Q (bad) optical cavity (frequency ω_L). This cavity is resonantly coupled with the $|2\rangle = 6p^2P_{1/2} - |3\rangle = 7s^2S_{1/2}$ transition in ^{133}Cs . A sufficient driving strength creates the population inversion between two atomic states and, as a result, the lasing action occurs. Due to the substantial suppression of the cavity pulling effect, this bad-cavity laser is operated as an active optical clock at $\lambda_{\text{clock2}} = 1359$ nm [7]. The other sub-beam of the laser source (i.e., passive optical clock) is coupled into the microcavity II, where an optical frequency

comb (microcomb) is created via the nonlinear Kerr process. The beat note between microcomb and active clock laser is used to control the light power launched into the microcavity II, thereby stabilizing the mode spacing of the microcomb [21].

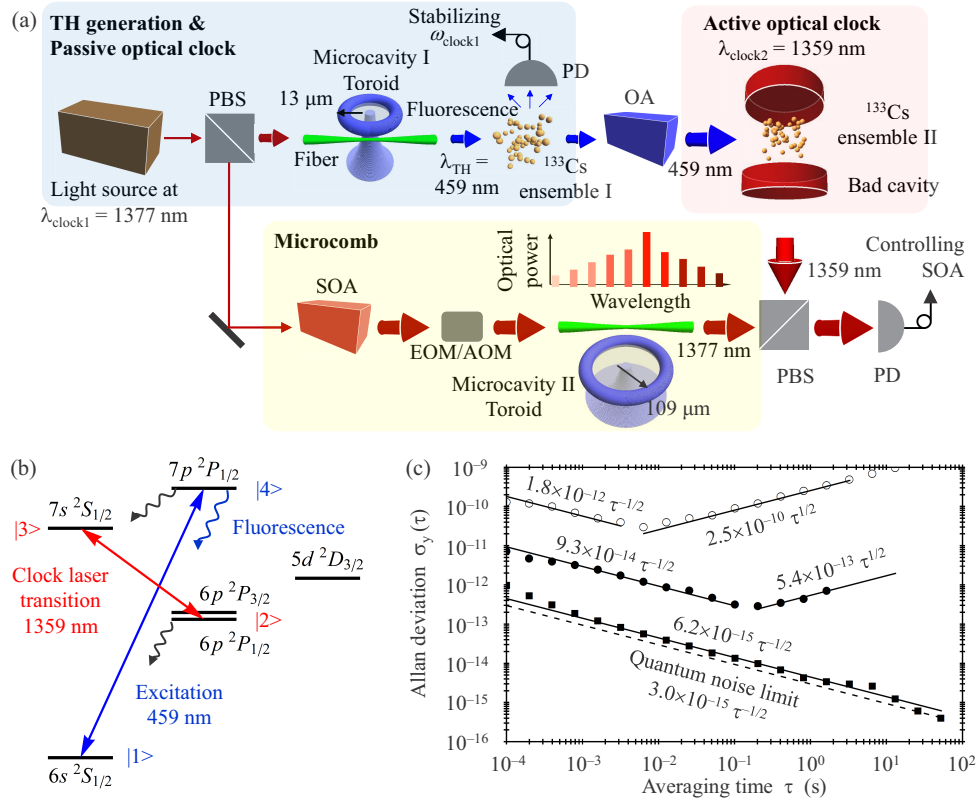


Fig. 1. Hybrid clock system. (a) Schematic diagram. One sub-beam from a light source at $\lambda_{\text{clock1}} = 1377 \text{ nm}$ undergoes the TH nonlinear process and drives the fluorescence of ^{133}Cs atoms. The light source serves as a passive optical clock when its frequency is stabilized using the fluorescence signal. The TH light further pumps an active clock laser at $\lambda_{\text{clock2}} = 1359 \text{ nm}$. The other sub-beam from the light source pumps a Kerr microcomb. (b) Energy-level structure of ^{133}Cs . The $6s^2S_{1/2} - 7p^2P_{1/2}$ transition serves as the frequency reference line for the passive optical clock and the pump line for the active optical clock. The $6p^2P_{1/2} - 7s^2S_{1/2}$ transition plays the role of the active clock laser transition. (c) Allan deviation of the free-running light source (open circles), the passive optical clock (filled circles), and the active optical clock (filled squares). Solid curves: curve fitting. Dashed line: quantum noise limit.

In our hybrid scheme, two atomic ensembles play different roles, where the ensemble I is used to stabilize the central frequency of the passive optical clock while the ensemble II acts as the optical gain medium for the active clock laser. Figure 1(b) depicts the energy level structure of ^{133}Cs . For simplicity, here we do not consider the hyperfine structure of ^{133}Cs . The atomic $|1\rangle - |4\rangle$ transition at 459 nm is used as the indirect frequency reference for the passive optical clock and the pump line for the active optical clock. The atomic $|2\rangle - |3\rangle$ transition at 1359 nm works as the laser transition that couples to the bad cavity. We use γ_{ij} with $(i, j = 1, 2, 3, 4)$ to denote the (effective) decay rate of the atom from $|i\rangle$ to $|j\rangle$ with $\gamma_{21} = 2\pi \times 4.6 \text{ MHz}$, $\gamma_{31} = 2\pi \times 1.8 \text{ MHz}$, $\gamma_{32} = 2\pi \times 1.0 \text{ MHz}$, $\gamma_{41} = 2\pi \times 0.5 \text{ MHz}$, $\gamma_{42} = 2\pi \times 0.02 \text{ MHz}$, and $\gamma_{43} = 2\pi \times 0.6 \text{ MHz}$ [22]. It should be noted that although, for example, the $|1\rangle - |3\rangle$ transition is electric-dipole forbidden,

atoms in $|3\rangle$ can decay to $|1\rangle$ through the spontaneous emission from $|3\rangle$ to $6p^2P_{3/2}$ and further to $|1\rangle$, leading to the effective decay rate γ_{31} . In this work, we assume that two atomic ensembles have been carefully engineered such that Doppler effect and interatomic collisions are negligible.

In what follows, we discuss the passive and active optical clocks and the microcomb in detail.

3. Third harmonic generation and passive optical clock

The light at $\lambda_{\text{TH}} = 459$ nm can be generated through the TH nonlinear optical process in the silica WGM microcavity I (for example, toroid with a major radius of $13\ \mu\text{m}$ and a minor radius of $3\ \mu\text{m}$ [12]), where the sub-beam (power P and frequency ω_{clock1}) from the light source excites a WGM that we label with "p" (frequency ω_p and quality factor Q_p) at 1377 nm via a tapered optical fiber and the TH optical wave is resonant to a WGM that we label with "s" (frequency ω_s and quality factor Q_s), as shown in Fig. 1(a). We write the intracavity fields of the two WGMs as $E_{j=p,s}(\mathbf{r}, t) = \frac{1}{2}a_j(t)\psi_j(\mathbf{r})e^{-i\omega_j t}$ with amplitudes $a_j(t)$ and normalized WGMs $\psi_j(\mathbf{r})$. It is convenient to introduce the amplitudes $b_j(t) = [\frac{\epsilon_0}{2} \int n_j^2 |\psi_j(\mathbf{r})|^2 d\mathbf{r}]a_j(t)$ with the vacuum permittivity ϵ_0 and refractive indices n_j , and $|b_j(t)|^2$ correspond to the intracavity energies of two fields. The coupling dynamics between $b_p(t)$ and $b_s(t)$ is described by [23]

$$\dot{b}_s(t) = [-\omega_s/(2Q_s) + i(3\omega_{\text{clock1}} - \omega_s)]b_s + i3\gamma_{\text{TH}}b_p^3, \quad (1)$$

$$\dot{b}_p(t) = [-\omega_p/(2Q_p) + i(\omega_{\text{clock1}} - \omega_p)]b_p + i\gamma_{\text{TH}}^*b_s(b_p^*)^2 + i\sqrt{\kappa_p P}, \quad (2)$$

where the nonlinear TH coefficient takes the form $\gamma_{\text{TH}} = \frac{\omega_s \chi_{\text{TH}}}{2\epsilon_0} \int \psi_s^*(\mathbf{r})\psi_p^3(\mathbf{r})d\mathbf{r}$ with the TH susceptibility $\chi_{\text{TH}} \sim 10^{-22}$ m² V⁻² for fused silica [24] and $\kappa_p (< \frac{\omega_p}{Q_p})$ is the coupling rate of the pump beam into the microcavity I. The condition of energy conservation requires $\omega_s = 3\omega_p$. The WGM dispersion caused by different high-order transverse modes compensates the material dispersion, ensuring the phase matching condition [12].

In the steady state (ss), one obtains $(1 + xy^4)y = 1$ with $x = 3(\frac{2Q_s}{\omega_s})(\frac{2Q_p}{\omega_p})^5(|\gamma_{\text{TH}}|\kappa_p P)^2$ and $y = (\frac{\omega_p}{2Q_p})\frac{|b_{p,ss}|}{\sqrt{\kappa_p P}}$ for the resonant pump $\omega_{\text{clock1}} = \omega_p$. The TH conversion efficiency is then given by $\eta_{\text{TH}} = \kappa_s \frac{|b_{s,ss}|^2}{3P} = (\frac{\kappa_s Q_s}{\omega_s})(\frac{\kappa_p Q_p}{\omega_p})4xy^6$. Here, we have defined $b_{j,ss} = b_j(t \rightarrow \infty)$ with $j = p, s$ and $\kappa_s (< \frac{\omega_s}{Q_s})$ accounts for the coupling rate of the TH signal out of the microcavity I. The efficiency η_{TH} reaches its maximum $\max(\eta_{\text{TH}}) = (\frac{\kappa_s Q_s}{\omega_s})(\frac{\kappa_p Q_p}{\omega_p})$ when $x = 16$ and $y = 1/2$ (Supplement 1). Generally, the pump mode is a fundamental WGM and κ_p is equal to half of $\frac{\omega_p}{Q_p}$ under the critical coupling point [25]. In contrast, the TH coupling efficiency is relatively low because of the high-order transverse mode. Substituting typical values $Q_{s,p} = 10^7$, $\frac{\kappa_s Q_s}{\omega_s} = 0.5\%$, and $\gamma_{\text{TH}} = 7 \times 10^{18}$ J⁻¹ s⁻¹, we have $\max(\eta_{\text{TH}}) = 0.25\%$ with the corresponding pump power $P = 2.8$ mW. The resultant output power of the TH light reaches $\kappa_s |b_{s,ss}|^2 = 7.0\ \mu\text{W}$.

In practice, environmental noise perturbs the frequencies of light source and WGMs, $\omega_{\text{clock1}} = \omega_{\text{clock1},0} + \delta\omega_{\text{clock1}}(t)$, $\omega_p = \omega_{p,0} + \delta\omega_p(t)$, and $\omega_s = \omega_{s,0} + \delta\omega_s(t)$ with constant values $(\omega_{\text{clock1},0}, \omega_{p,0}, \omega_{s,0})$ and fluctuations $(\delta\omega_{\text{clock1}}(t), \delta\omega_p(t), \delta\omega_s(t))$. The TH generation requires $\omega_{s,0} = 3\omega_{p,0}$. Generally, the frequency noise spectrum of the free-running light source $S_{\text{clock1}}(f) = \omega_{\text{clock1},0}^{-2} \int \langle \delta\omega_{\text{clock1}}(t)\delta\omega_{\text{clock1}}(t+\tau) \rangle e^{-i2\pi f\tau} d\tau$ takes the form $S_{\text{clock1}}(f) = h_{\text{clock1},0}f^0 + h_{\text{clock1},-2}f^{-2}$. The white frequency component ($\propto f^0$) determines the laser linewidth $\Delta\omega_{\text{clock1}} = \omega_{\text{clock1},0}^2 h_{\text{clock1},0}/2$ while the random walk component ($\propto f^{-2}$) leads to the long-term drift of the laser frequency. The typical $\Delta\omega_{\text{clock1}} = 2\pi \times 1$ MHz gives $h_{\text{clock1},0} = 6.7 \times 10^{-24}$ s and the corresponding short-term Allan deviation is $\sigma_y(\tau) = \sqrt{h_{\text{clock1},0}/2\tau} = 1.8 \times 10^{-12}\tau^{-1/2}$. Similarly, we have the frequency noise spectra of two WGMs [26], $S_p(f) = \omega_{p,0}^{-2} \int \langle \delta\omega_p(t)\delta\omega_p(t+$

$\tau\rangle)e^{-i2\pi f\tau}d\tau = h_{p,0}f^0 + h_{p,-2}f^{-2}$ and $S_s(f) = \omega_{s,0}^{-2} \int \langle \delta\omega_s(t)\delta\omega_s(t+\tau) \rangle e^{-i2\pi f\tau} d\tau = h_{s,0}f^0 + h_{s,-2}f^{-2}$ with $h_{p,0} = \frac{2}{Q_p\omega_{p,0}} = 1.5 \times 10^{-22}$ s and $h_{s,0} = \frac{2}{Q_s\omega_{s,0}} = 5.0 \times 10^{-23}$ s. For simplicity, we assume $h_{-2} = h_{\text{clock1},-2} = h_{p,-2} = h_{s,-2} = 1.0 \times 10^{-20}$ s⁻¹ with the corresponding long-term Allan deviation $\sigma_y(\tau) = \sqrt{2\pi^2 h_{-2} \tau / 3} = 2.5 \times 10^{-10} \tau^{1/2}$.

The absolute frequency ω_{clock1} of the light source may be indirectly stabilized to an atomic transition. We let the output TH light $\sqrt{\kappa_s}b_s$ (frequency $\omega_{\text{TH}} = 2\pi c/\lambda_{\text{TH}} = 3\omega_{\text{clock1}}$) further derive the $|1\rangle - |4\rangle$ transition (frequency ω_{41}) of the ¹³³Cs ensemble I (atom number N_{at}). The dynamics of atomic variables is governed by the following c -number Langevin equations [27] (Supplement 1)

$$\dot{N}_1(t) = \gamma_{21}N_2 + \gamma_{31}N_3 + \gamma_{41}N_4 + (\Omega^*M_{14} + \Omega M_{14}^*) + F_{N_1}(t), \quad (3)$$

$$\dot{N}_2(t) = -\gamma_{21}N_2 + \gamma_{32}N_3 + \gamma_{42}N_4 + F_{N_2}(t), \quad (4)$$

$$\dot{N}_3(t) = -(\gamma_{31} + \gamma_{32})N_3 + \gamma_{43}N_4 + F_{N_3}(t), \quad (5)$$

$$\dot{N}_4(t) = -(\gamma_{41} + \gamma_{42} + \gamma_{43})N_4 - (\Omega^*M_{14} + \Omega M_{14}^*) + F_{N_4}(t), \quad (6)$$

$$\dot{M}_{14}(t) = [-\Gamma_{41} + i(\omega_{\text{TH}} - \omega_{41})]M_{14} + \Omega(N_4 - N_1) + F_{M_{14}}(t), \quad (7)$$

where $N_{j=1,2,3,4}$ denotes the population of atoms in the atomic $|j\rangle$ state and M_{14} accounts for the macroscopic polarization corresponding to the atomic $|1\rangle - |4\rangle$ transition whose decoherence rate is $\Gamma_{41} = 2(\gamma_{41} + \gamma_{42} + \gamma_{43})$. Fluctuations $F_\alpha(t)$ with $\alpha = N_{1,2,3,4}$ and M_{14} originate from the spontaneous emission of atoms and follow the correlation functions $\langle F_\alpha(t) \rangle = 0$ and $\langle F_\alpha(t)F_\beta(t') \rangle = 2D(\alpha, \beta)\delta(t - t')$. All nonvanishing diffusion coefficients $2D(\alpha, \beta)$ are listed in Supplement 1. The Rabi frequency is defined as $\Omega = -\sqrt{\frac{2\kappa_s}{\epsilon_0 c A_{\text{TH}}}} \frac{d_{41}b_s}{2\hbar}$ with the effective area A_{TH} of the TH beam and the reduced Planck constant \hbar . The transition dipole moment d_{41} of the atomic $|1\rangle - |4\rangle$ transition is computed to be $0.18 ea_0$ with the elementary charge e and the Bohr radius a_0 . The conservation of atoms leads to $\sum_{i=1}^4 N_i = N_{at}$. We choose a TH beam waist radius of 0.6 mm, an atom–light interaction length of 2 cm, and an atomic density of 10^{10} cm⁻³, resulting in $N_{at} = 2.5 \times 10^8$ and $A_{\text{TH}} = 1$ mm².

Dropping fluctuation terms $\delta\omega_{\text{clock1},p,s}(t)$ and $F_\alpha(t)$ with $\alpha = N_{1,2,3,4}$ and M_{14} in Eqs. (1)–(7), one may compute the dependence of the steady-state population $N_{4,ss} = N_4(t \rightarrow \infty)$ of atoms in $|4\rangle$ on the pump detuning $\Delta_p = \omega_{\text{clock1},0} - \omega_{p,0}$. As shown in Fig. 2, the atomic excitation exhibits a Lorentzian lineshape with a full width at half maximum (FWHM) $\Gamma_p = 2\pi \times 1.4$ MHz, close to the natural linewidth of the $|1\rangle - |4\rangle$ transition. Atoms in $|4\rangle$ emit fluorescent photons at 459 nm, which are measured by a photodetector (PD). Detecting fluorescence allows for locking the frequency $\omega_{\text{clock1}}(t)$ to the atomic $|1\rangle - |4\rangle$ transition in an indirect manner. We set the locking point at $\Delta_p = -\Gamma_p/2$, where the gradient of the frequency discrimination curve is $k = dN_{4,ss}/d\Delta_p = 0.44$ s.

According to the frequency noise spectra ($S_{\text{clock1}}(f)$, $S_p(f)$, $S_s(f)$), one may numerically produce the frequency fluctuations ($\delta\omega_{\text{clock1}}(t)$, $\delta\omega_p(t)$, $\delta\omega_s(t)$) by digitally filtering a stochastic white field [28]. Langevin forces $F_\alpha(t)$ with $\alpha = N_{1,2,3,4}$ and M_{14} can be generated following the method in [29,30] (Supplement 1). Thus, we simulate the frequency stabilization of the light source based on Eqs. (1)–(7). The integration time of the detection electronics is set to be $T_i = 0.1$ ms. Within the time period from nT_i to $(n+1)T_i$ with $n \in \mathbb{Z}$, the number of fluorescent photons collected by the photodetector is $N_{ph} = \gamma_{41} \int N_4(t)dt + \Delta N_{ph}$. The extra term ΔN_{ph} is a random number that originates from the shot noise whose mean is zero and standard deviation is $N_{ph}^{1/2}$. Here, we have assumed 100-percent efficiency of the photon detection. The average value of $\delta\omega_{\text{clock1}}(t)$ within this integration period is then derived as $\langle \delta\omega_{\text{clock1}} \rangle_{T_i} = (N_{ph} - N_{ph,bia})/(k\gamma_{41}T_i)$, where $N_{ph,bia}$ denotes the steady-state number of fluorescent photons at the locking point. As a result, the light source frequency ω_{clock1} is corrected accordingly in the next integration period.

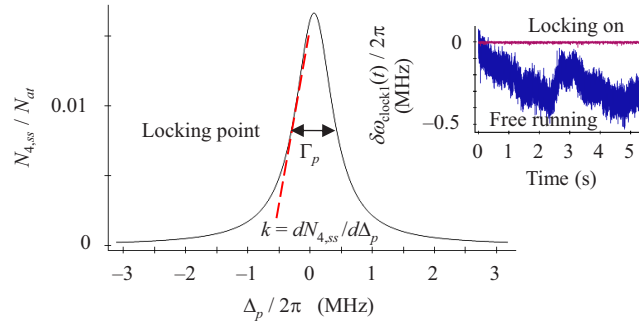


Fig. 2. Dependence of the fluorescence response on the pump detuning $\Delta_p = \omega_{\text{clock1},0} - \omega_{p,0}$. The frequency $\omega_{\text{clock1}}(t)$ of the light source is locked to the side of the fluorescence curve. The dashed line corresponds to the gradient $k = dN_{4,ss}/d\Delta_p$ at the locking point. Inset: Frequency fluctuations $\delta\omega_{\text{clock1}}(t)$ of the free-running/frequency-locked light source. The stabilized light source is operated as a passive optical clock.

The Allan deviation $\sigma_y(\tau)$ of the simulated ω_{clock1} is summarized in Fig. 1(c). The free-running ω_{clock1} follows the short-term $\sigma_y(\tau) = 1.8 \times 10^{-12} \tau^{-1/2}$ and the long-term $\sigma_y(\tau) = 2.5 \times 10^{-10} \tau^{1/2}$. In contrast, the stabilized ω_{clock1} obeys the short-term $\sigma_y(\tau) = 9.3 \times 10^{-14} \tau^{-1/2}$, over one order of magnitude better than that of the free-running laser, and the long-term $\sigma_y(\tau) = 5.2 \times 10^{-13} \tau^{1/2}$, corresponding to an improvement factor of about 500. Consequently, the light source at λ_{clock1} is operated as an optical frequency standard whose frequency is passively stabilized to the atomic $|1\rangle - |4\rangle$ transition in an indirect manner. The short-term stability is better than the recently demonstrated compact optical atomic clock, where a 1556-nm laser beam is frequency doubled (via the second harmonic generation) and further stabilized to the 778-nm two-photon transition in rubidium [31]. We compute the stability limit set by atomic fluctuations, $\sigma_y(\tau) = \frac{\Gamma_p}{\omega_{\text{clock1},0}} \frac{1}{\text{SNR}} \sqrt{\frac{T_i}{\tau}} = 9.1 \times 10^{-14} \tau^{-1/2}$ with the signal-to-noise ratio $\text{SNR} = \frac{N_{4,ss}}{2} \sqrt{\frac{\Gamma_{41}}{2D(N_4, N_4)}}$ and the diffusion coefficient $2D(N_4, N_4)$ associated with the population N_4 of atoms in $|4\rangle$ (Supplement 1). In addition, the stability limited by the photon shot noise is evaluated as $\sigma_y(\tau) = \frac{\Gamma_p}{\omega_{\text{clock1},0}} \frac{1}{\sqrt{N_{ph}}} \sqrt{\frac{T_i}{\tau}} = 3.1 \times 10^{-15} \tau^{-1/2}$. Therefore, the stability of the passive optical clock is primarily limited by atomic fluctuations.

4. Active optical clock

As shown in Fig. 1(a), after passing an optical amplifier (OA), the TH light $\sqrt{\kappa_s} b_s$ interacts with the ^{133}Cs ensemble II. For simplicity, we still use the symbols $N_{i=1,2,3,4}$, M_{14} , N_{at} , and Ω to denote the population of atoms in $|i\rangle$, the macroscopic polarization corresponding to the $|1\rangle - |4\rangle$ transition, the atom number, and the driving strength. Here, we assume that the frequency ω_{TH} of the TH light has been shifted to ω_{41} . Atoms in $|1\rangle$ are excited to $|4\rangle$ and then decay to $|3\rangle$, creating the population inversion between $|2\rangle$ and $|3\rangle$. A low- Q cavity (frequency ω_L and loss rate κ_L) is coupled with the $|2\rangle - |3\rangle$ transition (frequency ω_{32} and transition dipole moment $d_{32} = 1.6 ea_0$) with the single-photon coupling strength $g = -\sqrt{\frac{\omega_L}{2\hbar\epsilon_0 V_L}} d_{32} = -2\pi \times 10$ kHz and the cavity mode volume $V_L = \pi(0.5 \text{ mm})^2(5 \text{ cm})$. The lasing action (wavelength $\lambda_{\text{clock2}} = 1359$ nm) occurs once the optical gain overcomes optical losses. Following the Heisenberg–Langevin approach [27], the equations of motion of intracavity field A and atomic variables are derived as (Supplement 1)

$$\dot{A}(t) = [-\kappa_L/2 - i(\omega_L - \omega_{32})]A + gM_{23}, \quad (8)$$

$$\dot{N}_1(t) = \gamma_{21}N_2 + \gamma_{31}N_3 + \gamma_{41}N_4 + (\Omega^* M_{14} + \Omega M_{14}^*) + F_{N_1}(t), \quad (9)$$

$$\dot{N}_2(t) = -\gamma_{21}N_2 + \gamma_{32}N_3 + \gamma_{42}N_4 + g(M_{23}^*A + A^*M_{23}) + F_{N_2}(t), \quad (10)$$

$$\dot{N}_3(t) = -(\gamma_{31} + \gamma_{32})N_3 + \gamma_{43}N_4 - g(M_{23}^*A + A^*M_{23}) + F_{N_3}(t), \quad (11)$$

$$\dot{N}_4(t) = -(\gamma_{41} + \gamma_{42} + \gamma_{43})N_4 - (\Omega^*M_{14} + \Omega M_{14}^*) + F_{N_4}(t), \quad (12)$$

$$\dot{M}_{14}(t) = [-\Gamma_{41} + i(\omega_{\text{TH}} - \omega_{41})]M_{14} + \Omega(N_4 - N_1) + F_{M_{14}}(t), \quad (13)$$

$$\dot{M}_{23}(t) = -\Gamma_{32}M_{23} + g(N_3 - N_2)A + F_{M_{23}}(t), \quad (14)$$

where M_{23} represents the macroscopic polarization corresponding to the $|2\rangle - |3\rangle$ transition and $\Gamma_{32} = (\gamma_{21} + \gamma_{31} + \gamma_{32})/2$ is the decoherence rate of M_{23} . Fluctuations $F_\alpha(t)$ with $\alpha = N_{1,2,3,4}$ and $M_{14,23}$ follow the correlation functions $\langle F_\alpha(t) \rangle = 0$ and $\langle F_\alpha(t)F_\beta(t') \rangle = 2D(\alpha, \beta)\delta(t - t')$. All nonvanishing diffusion coefficients $2D(\alpha, \beta)$ are listed in [Supplement 1](#). As we will see below, this laser has an outstanding frequency stability in the bad-cavity limit ($\kappa_L \gg \Gamma_{32}$) due to the substantial suppression of the cavity pulling effect [7]. Thus, the laser directly serves as an optical frequency standard, i.e., an active optical clock.

Let us first consider the steady state of the laser system in the resonant coupling situation, $\omega_L = \omega_{32}$ and $\omega_{\text{TH}} = \omega_{41}$. The corresponding analytical solutions are given in [Supplement 1](#). Figures 3(a) and (b) illustrate the dependence of the output power $P_{\text{clock2}} = \kappa_L \hbar \omega_L |A_{\text{ss}}|^2$ with $A_{\text{ss}} = A(t \rightarrow \infty)$ and the laser linewidth $\Delta\omega_{\text{clock2}}$ on the cavity loss rate κ_L and the atom number N_{at} . In the good-cavity regime ($\kappa_L < \Gamma_{32}$), the required minimal N_{at} for the lasing action can be small, for example, $N_{\text{at}} \sim 10^5$ with $\kappa_L/\Gamma_{32} = 0.1$, corresponding to $Q_L = \omega_L/\kappa_L = 5 \times 10^8$. The linewidth $\Delta\omega_{\text{clock2}}$ reaches the Hz level (or even less than 1 Hz). However, in this regime the central frequency of the clock laser suffers huge cavity frequency fluctuations through the cavity pulling effect, consequently deteriorating the laser frequency stability [32]. As κ_L grows, the increased cavity loss strongly elevates the threshold and $\Delta\omega_{\text{clock2}}$ also goes up. Nevertheless, in the bad-cavity regime ($\kappa > \Gamma_{32}$), P_{clock2} can exceed 1 μW , which is high enough for locking the phase of an optical local oscillator. Interestingly, once the system enters the bad-cavity regime, $\Delta\omega_{\text{clock2}}$ starts declining as κ_L is increased. According to [33], the quantum-limited linewidth of a laser takes the form $\Delta\omega_{\text{clock2}} = \Delta\omega_{\text{ST}}(1 + \kappa_L/2\Gamma_{32})^{-2}$ with the usual Schawlow–Townes linewidth $\Delta\omega_{\text{ST}}$. When $\kappa_L \gg \Gamma_{32}$, the factor $(1 + \kappa_L/2\Gamma_{32})^{-2}$ decreases rapidly, thereby suppressing $\Delta\omega_{\text{clock2}}$. The underlying mechanism may be ascribed to the fact that the phase diffusion process gets slowed down due to the memory effect of the relatively long-lifetime polarization of atoms [34]. We choose $N_{\text{at}} = 2.5 \times 10^8$, i.e., the two atomic ensembles have the same atom number. As shown in Fig. 3(c), in the bad-cavity regime $\Delta\omega_{\text{clock2}}$ reaches its minimum $\min(\Delta\omega_{\text{clock2}}) = 2\pi \times 2.8$ Hz at $\kappa/\Gamma_{32} = 90$, where, in what follows, we set the operating point of the active clock laser. The corresponding cavity quality factor is $Q_L = 6 \times 10^5$ and the output power P_{clock2} approximates 20 μW .

We now consider the frequency stability of the active clock laser. In the adiabatic approximation, $\kappa_L \gg \Gamma_{41,32}$, one has $A(t) = [\kappa_L/2 + i(\omega_L - \omega_{32})]^{-1} gM_{23}(t)$. It is seen that two factors, noise in $\omega_L(t) = \omega_{L,0} + \delta\omega_L(t)$ and fluctuations of the polarization M_{23} , influence $A(t)$. The resonant atom–cavity coupling gives $\omega_{L,0} = \omega_{32}$. Generally, the power spectral density of the cavity frequency noise $S_L(f) = \omega_{L,0}^{-2} \int \langle \delta\omega_L(t)\delta\omega_L(t + \tau) \rangle e^{-i2\pi f\tau} d\tau$ takes the form $S_L(f) = h_{L,0}f^0 + h_{L,-1}f^{-1} + h_{L,-2}f^{-2}$ with $h_{L,0} = 2\kappa_L/\omega_{L,0}^2 = 2.3 \times 10^{-21}$ s. Here, we ignore the flicker frequency noise component ($\propto f^{-1}$), which originates from Brownian thermal-mechanical fluctuations of cavity mirrors, due to the low Q_L and assume $h_{L,-2} = h_{-2}$. One may simulate the dynamics of the active optical clock by numerically generating the frequency noise $\delta\omega_L(t)$ and Langevin fluctuations $F_\alpha(t)$ with $\alpha = N_{1,2,3,4}$ and $M_{14,23}$ according to $S_L(f)$ and diffusion coefficients $2D(\alpha, \beta)$ of atomic variables ([Supplement 1](#)). Figure 3(d) depicts the laser spectrum $S_{\text{clock2}}(\omega) = \int \langle A(t)A(t + \tau) \rangle e^{-i\omega\tau} d\tau$ in the absence of fluctuations in ω_L and b_s . The corresponding spectral broadening completely arises from the fluctuations associated with atomic variables. The curve fitting gives the FWHM of $2\pi \times 3$ Hz, well matching the analytical result of $2\pi \times 2.8$ Hz and verifying

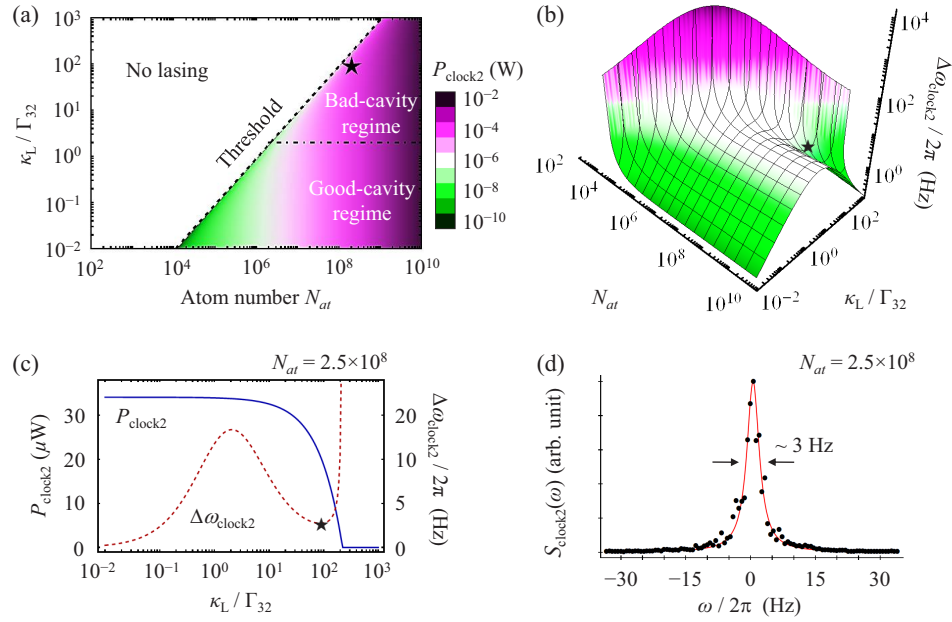


Fig. 3. Steady state of the active optical clock. (a) Dependence of the output power P_{clock2} on the cavity loss rate κ_L and the atom number N_{at} . The dashed line denotes the laser threshold. The dash-dotted line corresponds to the boundary between good- and bad-cavity regimes. (b) Laser linewidth $\Delta\omega_{\text{clock2}}$ vs. $(N_{\text{at}}, \kappa_L)$. (c) Dependence of P_{clock2} and $\Delta\omega_{\text{clock2}}$ on κ_L with $N_{\text{at}} = 2.5 \times 10^8$. The five-pointed star symbol: The operating point of the active optical clock is set at $\kappa_L/\gamma_{32} = 90$, where $P_{\text{clock2}} = 20 \mu\text{W}$ and $\Delta\omega_{\text{clock2}} = 2\pi \times 2.8 \text{ Hz}$ (five-pointed star symbol in (a) and (b)). (d) Power density spectrum of the active clock laser at the operating point. The curve fitting gives the FWHM of $2\pi \times 3 \text{ Hz}$. For all plots, the pump strength is $|\Omega|/\Gamma_{41} = 5$.

the validity of the simulation. Since this $\Delta\omega_{\text{clock2}}$ is entirely induced by atomic fluctuations, the corresponding Allan deviation $\sigma_y(\tau) = \omega_{\text{clock2},0}^{-1} (\Delta\omega_{\text{clock2}}/\tau)^{1/2} = 3.0 \times 10^{-15} \tau^{-1/2}$ is referred to as the quantum-noise-limited stability.

Considering the fluctuations in ω_L and b_s , we perform the long-term simulation of the active clock dynamics, compute the clock frequency ω_{clock2} (see Supplement 1), and evaluate its Allan deviation. The simulation result is $\sigma_y(\tau) = 6.2 \times 10^{-15} \tau^{-1/2}$ (see Fig. 1(c)), which is higher than the quantum-noise-limited stability due to the residual cavity-pulling effect. As we will see below, this active optical clock can be used to stabilize a Kerr microcomb.

5. Microcomb

Thus far, we have only considered one sub-beam from the light source (i.e., passive optical clock). As shown in Fig. 1(a), the other sub-beam whose power is enhanced using a semiconductor optical amplifier (SOA) drives a certain mode (i.e., pump mode) in the silica microcavity II that may be a toroid microresonator (major radius of $109 \mu\text{m}$ and minor radius of $3 \mu\text{m}$). A sufficient input power excites multiple WGMs with stable phases around the pump mode through the nonlinear Kerr process and four-wave mixing [37], forming an optical frequency microcomb [38]. For the sake of simplicity, we still use the symbols ω_p , Q_p , and $\Delta_p = \omega_{\text{clock1}} - \omega_p$ to denote the pump mode frequency, the corresponding quality factor, and the detuning between the passive clock laser and the pump mode, respectively.

The dynamics of the microcomb field $E_{\text{comb}}(t, \theta)$ (in units of $\text{W}^{1/2}$) is governed by the Lugiato–Lefever equation [39]

$$\frac{\partial}{\partial t} E_{\text{comb}}(t, \theta) = \left[-\frac{\omega_p}{2Q_p} + i\Delta_p - i\frac{L}{\tau_R} \frac{\beta}{2} \frac{\partial^2}{\partial \theta^2} + i\frac{L}{\tau_R} \gamma_{\text{Kerr}} |E_{\text{comb}}(t, \theta)|^2 \right] E_{\text{comb}}(t, \theta) + \frac{\sqrt{P}}{\tau_R}, \quad (15)$$

with the slow time t , the fast phase $0 < \theta < 2\pi$, the dispersion coefficient $\beta = (2\pi/\tau_R)^2 \text{GVD}$, the round-trip duration $\tau_R = L/v_g$, the microcavity circumference L , the group velocity v_g , and the group dispersion GVD. The nonlinear Kerr coefficient is given by $\gamma_{\text{Kerr}} = \frac{8\pi n_0 n_2}{3A_{\text{eff}} \lambda_{\text{clock1}}}$ with the refractive index n_0 , the second-order nonlinear refractive index n_2 , and the effective cross-section area A_{eff} of the pump mode. Varying SOA tunes the input pump power P launched into the microcavity II. Indeed, both v_g and GVD are linked to the group refractive index $n_g(\omega, T) = n(\omega, T) + \omega \frac{\partial n(\omega, T)}{\partial \omega}$, i.e., $v_g = c/n_g$ and $\text{GVD} = \frac{\partial}{\partial \omega} \frac{1}{v_g}$. The common refractive index $n(\omega, T)$ of the medium depends on the optical frequency ω and the temperature T . We compute n_g according to [40,41] (see Fig. 4(a)). Table 1 lists the relevant physical parameters of the microcomb at λ_{clock1} and room temperature $T_0 = 293$ K.

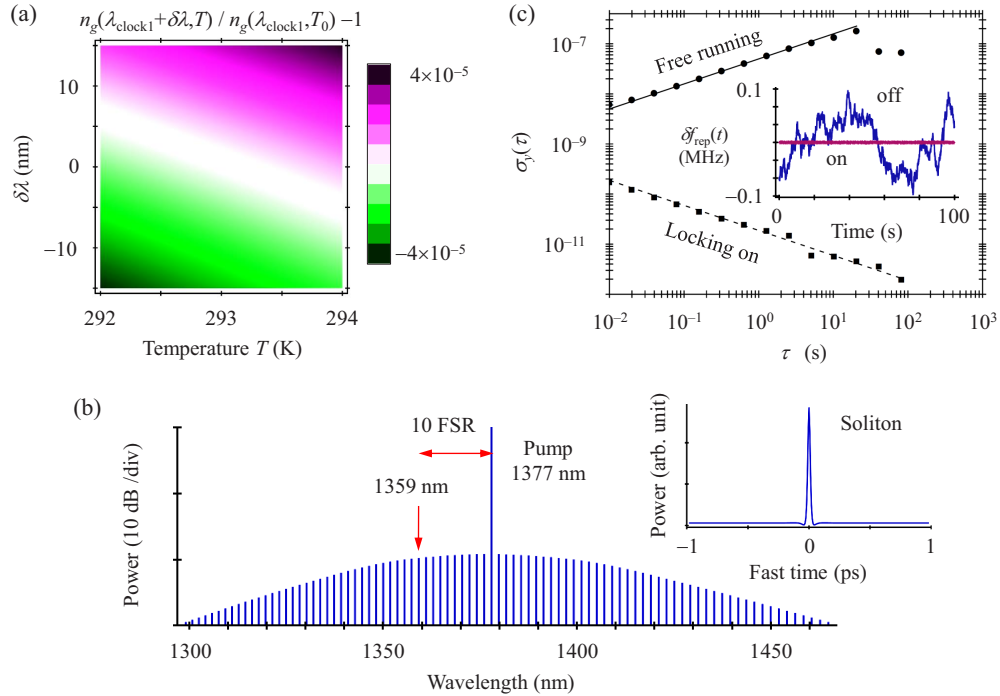


Fig. 4. Kerr microcomb. (a) Dependence of the group refractive index n_g on the wavelength change $\delta\lambda = \lambda - \lambda_{\text{clock1}}$ and temperature T around ($\lambda_{\text{clock1}} = 1377$ nm, $T_0 = 293$ K). (b) Single-soliton microcomb. The 10th comb mode on the blue-detuned side of the pump mode is near resonant to the active optical clock. Inset: single soliton. (c) Allan deviation $\sigma_y(\tau)$ of the mode spacing $f_{\text{rep}}(t)$ for the microcomb in the free-running/stabilized state. Inset: fluctuations $\delta f_{\text{rep}}(t)$ of the mode spacing when the feedback loop is switched off/on.

Figure 4(b) shows the microcomb spectrum that is numerically derived from Eq. (15) with the input power $P = 1.5$ mW and the detuning $\Delta_p = -3(\omega_p/Q_p)$. Multiple sidebands are located around the pump mode (corresponding to the highest peak). The entire microcomb is characterized by two degrees of freedom, namely the offset frequency of the carrier envelope

Table 1. Physical parameters of the microresonator-based optical frequency comb at λ_{clock1} and room temperature $T_0 = 293$ K.

Physical parameter	Symbol	Value
Circumference	L	$2\pi \times 109 \mu\text{m}$
Group dispersion	GVD	$-9.5 \text{ fs}^2 \text{ mm}^{-1}$
Group velocity	v_g	$2.1 \times 10^8 \text{ m s}^{-1}$
Round-trip duration	τ	3.3 ps
Dispersion coefficient	β	-0.034 m^{-1}
Free spectral range	FSR	0.3 THz
Refractive index	n_0	1.446
Second-order nonlinear refractive index	n_2	$2.5 \times 10^{-20} \text{ m}^2 \text{ W}^{-1}$ [35]
Effective cross-section area	A_{eff}	$1.8 \times 10^{-12} \text{ m}^2$ [36]
Kerr coefficient	γ_{Kerr}	$0.12 \text{ W}^{-1} \text{ m}^{-1}$
Quality factor of pump mode	Q_p	10^6

and the mode spacing (repetition frequency) f_{rep} . The microcomb is in the single-soliton state, leading to $f_{\text{rep}} = \text{FSR}$. The first degree of freedom has already been controlled since the passive optical clock directly drives one comb mode. Next we consider the stabilization of f_{rep} .

In practice, the temperature T fluctuates around T_0 . The small mode volume of the microcavity makes the mode spacing f_{rep} sensitive to the fluctuation $\delta T(t) = T - T_0$ that is averaged over the whole mode volume. In the linear approximation, the change of the group index n_g caused by δT is expressed as $\delta n_g = n_g(T) - n_g(T_0) = \eta_n \delta T$ with $\eta_n = \partial n_g(T_0) / \partial T = 1.6 \times 10^{-5} \text{ K}^{-1}$. Here, we neglect the thermo-mechanical effects that change the circulating length L . The induced fluctuation of f_{rep} is then written as $\delta f_{\text{rep}}(t) = -[\eta_n f_{\text{rep},0} / n_g(T_0)] \delta T(t)$ with $f_{\text{rep},0} = c / L n_g(T_0)$. According to the experimental results in [18,20], the typical Allan deviation of $y(t) = \delta f_{\text{rep}}(t) / f_{\text{rep},0}$ follows $\sigma_y(\tau > 5 \times 10^{-2} \text{ s}) = 5 \times 10^{-8} \tau^{1/2}$. Thus, the long-term drift of $\delta T(t)$ has $\sigma_y(\tau) = \sqrt{2\pi^2 h_{T,-2} \tau} / 3$ with $y(t) = \delta T(t) / T_0$ and $h_{T,-2} = 3.7 \times 10^{-11} \text{ s}^{-1}$. To verify this, we numerically generate the temperature fluctuations $\delta T(t)$ and compute the mode spacing $f_{\text{rep}}(t)$ by solving Eq. (15), where we have used $\text{GVD}(T) = \text{GVD}(T_0) + \eta_{\text{GVD}} \delta T$ with $\eta_{\text{GVD}} = -10.1 \text{ fs}^2 \text{ mm}^{-1} \text{ K}^{-1}$ and $\tau_R(T) = \tau_R(T_0) + \eta_\tau \delta T$ with $\eta_\tau = 3.7 \times 10^{-5} \text{ ps K}^{-1}$. In addition, the pump mode frequency can be approximated by $\omega_p(T) = \omega_p(T_0) + \eta_\omega \delta T$ with $\eta_\omega = -2\pi \times 2.4 \text{ GHz K}^{-1}$ and the stabilized clock frequency ω_{clock1} follows the Allan deviation shown in Fig. 1(c). The numerical $\sigma_y(\tau)$ of $\delta f_{\text{rep}}(t)$ is presented in Fig. 4(c), well matching the analytical expression.

In experiment, the change of the mode spacing can be derived by measuring the beat note $i_{\text{beat}}(t) = \text{Re}[A^*(t)E_m(t)]$ between the active optical clock $A(t)$ and its nearest mode $E_m(t)$, whose frequency is $\omega_p + m f_{\text{rep}}$ with $m = 10$, in the microcomb $E_{\text{comb}}(t, \theta)$. The beat frequency is set at $\omega_{\text{beat}} = 2\pi \times 50 \text{ MHz}$. We compare the beat note with a local RF signal at ω_{beat} and extract the phase difference $\Delta\phi$ over the integration time T_i of the detection electronics. Consequently, the average value $\langle \delta f_{\text{rep}} \rangle_{T_i}$ of $\delta f_{\text{rep}}(t)$ within T_i is given by $\langle \delta f_{\text{rep}} \rangle_{T_i} = \frac{\Delta\phi / T_i}{2\pi m} + \frac{\omega_{\text{beat}}}{2\pi m} \frac{\Delta N_{ph}}{\sqrt{\xi N_1 N_2}}$. The extra noise ΔN_{ph} represents the shot noise that has a zero mean and a standard deviation $\sqrt{N_1 + N_2}$ with $N_1 = (\frac{2Q_p}{\omega_p \tau_R})^2 [1 + (\frac{2\Delta_p Q_p}{\omega_p})^2]^{-1} \frac{P T_i}{2\hbar \omega_{\text{clock1}}}$ and $N_2 = \frac{P_{\text{clock2}} T_i}{\hbar \omega_{\text{clock2}}}$. Here, $\xi = 6.6 \times 10^{-3}$ accounts for the energy percentage of $E_m(t)$ in $E_{\text{comb}}(t, \theta)$ and we have assumed the critical coupling between the fiber and the microcavity II.

The dynamics of temperature fluctuations $\delta T(t)$ follows the equation [42]

$$\delta \dot{T}(t) = -\Gamma_T \delta T + \eta_T \delta \mathcal{E}(t) + F_T(t), \quad (16)$$

where $\Gamma_T = D/V_{\text{th}}$ denotes the thermal relaxation rate and $\eta_T = 2 \times 10^{14} \text{ K J}^{-1} \text{ s}^{-1}$ represents the photothermal heating coefficient. The fluctuations of the intracavity light energy $\delta\mathcal{E}(t) = \delta | \int E_{\text{comb}}(t, \theta) \frac{d\theta}{2\pi} |^2 \tau_R \approx (\frac{2Q_p}{\omega_p \tau_R})^2 [1 + (\frac{2\Delta_p Q_p}{\omega_p})^2]^{-1} \tau_R \delta P(t)$ originate from the fluctuations $\delta P(t)$ of the input power. Here, $D = 9.5 \times 10^{-7} \text{ m}^2 \text{ s}^{-1}$ corresponds to the thermal diffusivity and $V_{\text{th}} = 2 \times 10^{-14} \text{ m}^3$ is the effective thermal volume of the microcavity, leading to $\Gamma_T = 2\pi \times 4 \text{ MHz}$. The correlation function of thermal fluctuations $F_T(t)$ is given by $\langle F_T(t) F_T(t') \rangle = \frac{2\Gamma_T k_B T_0^2}{\rho C V_{\text{th}}} \delta(t - t')$ with the Boltzmann constant k_B , the material density $\rho = 2200 \text{ kg m}^{-3}$, and the specific heat capacity $C = 670 \text{ J kg}^{-1} \text{ K}^{-1}$. From Eq. (16), one may derive the noise spectrum of temperature fluctuations $S_T(f) = \int \langle \delta T(t) \delta T(t + \tau) \rangle e^{-i2\pi f \tau} d\tau \approx \frac{2\Gamma_T k_B T_0^2}{\rho C V_{\text{th}}} |\Gamma_T + i2\pi f|^{-2}$, where the component associated with $\delta\mathcal{E}(t)$ has been omitted. Thus, the thermal-noise-limited stability of the mode spacing $f_{\text{rep}}(t)$, i.e., Allan deviation $\sigma_y(\tau)$ of $y(t) = \delta f_{\text{rep}}(t)/f_{\text{rep},0}$, is given by $\sigma_y(\tau) = \eta_T f_{\text{rep},0} [2 \int_0^{T_i} S_T(f) \frac{\sin^4(\pi f \tau)}{(\pi f \tau)^2} df]^{1/2} \approx 6 \times 10^{-15} \tau^{-1/2}$. Generally, this thermal limit is well below the shot-noise-limited stability (see below). In addition, the time scale of interest in this work is much larger than the thermal dissipation scale $1/\Gamma_T$. Thus, we simplify Eq. (16) as $\delta T(t) = (\eta_T/\Gamma_T) \delta\mathcal{E}(t)$, that is, the temperature fluctuations is mainly caused by the pump power fluctuations. Controlling SOA (so as to control the pump power launched into the microcavity II) allows for stabilizing δT , thereby stabilizing δf_{rep} .

One may numerically simulate the stabilization of the mode spacing $f_{\text{rep}}(t)$. We firstly calculate the average value $\langle \delta f_{\text{rep}} \rangle_{T_i}$ of $\delta f_{\text{rep}}(t)$ within the integration time $T_i = 10^{-2} \text{ s}$. The temperature change averaged over T_i is then computed as $\langle \delta T \rangle_{T_i} = \langle \delta f_{\text{rep}} \rangle_{T_i} / (\eta_T f_{\text{rep},0}^2)$. The corresponding change of the light energy absorbed by the microcavity II reads $\langle \delta\mathcal{E} \rangle_{T_i} = (\Gamma_T/\eta_T) \langle \delta T \rangle_{T_i}$. Consequently, the input power P is corrected by $(\frac{\omega_p \tau_R}{2Q_p})^2 [1 + (\frac{2\Delta_p Q_p}{\omega_p})^2] \langle \delta\mathcal{E} \rangle_{T_i} / T_i$ for the next integration period. Numerical results are presented in Fig. 4(c). The Allan deviation of the stabilized $f_{\text{rep}}(t)$ follows $\sigma_y(\tau) = 1.9 \times 10^{-11} \tau^{-1/2}$, matching the shot-noise limit $\sigma_y(\tau) = \frac{\omega_{\text{beat}}}{2\pi m f_{\text{rep},0}} \sqrt{\frac{N_1 + N_2}{\xi N_1 N_2}} \sqrt{\frac{T_i}{\tau}} = 1.8 \times 10^{-11} \tau^{-1/2}$.

6. Discussion

In summary, we have proposed a hybrid clock scheme, where a passive optical clock pumps an active optical clock and a Kerr microcomb whose mode spacing is stabilized using the active optical clock. The passive optical clock is locked to one side of the fluorescence spectrum of the $6s^2 S_{1/2} - 7p^2 P_{1/2}$ transition in ^{133}Cs via the TH generation. The frequency stabilization may be improved by locking the clock frequency to the zero crossing point in the modulation transfer spectroscopy for ^{133}Cs [43]. The cancellation of Doppler broadening allows the use of thermal atoms, simplifying the preparation of the atomic ensemble. In particular, the passive optical clock can be miniaturized by confining ^{133}Cs atoms in a chip-scale vapor cell [16].

The active optical clock, i.e., bad-cavity laser, produces an infrared frequency standard that is located in the microcomb spectrum. The pump energy is supplied by the passive optical clock through the TH generation. Although in this work we focus on the atomic $6p^2 P_{1/2} - 7s^2 S_{1/2}$ (clock) and $6s^2 S_{1/2} - 7p^2 P_{1/2}$ (pump) transitions in ^{133}Cs , one may also choose the $6p^2 P_{3/2} - 7s^2 S_{1/2}$ clock transition at 1470 nm. In addition, the active optical clock scheme is applicable to rubidium atoms with clock $5p^2 P_{1/2,3/2} - 6s^2 S_{1/2}$ (wavelengths of 1323 and 1366 nm) and pump $5s^2 S_{1/2} - 6p^2 P_{1/2}$ (wavelength of 421 nm) transitions. Despite the absence of the Allan deviation measurement, active optical clocks have been demonstrated in [44,45] with thermal atoms. Employing cold atoms as the gain medium potentially improves the clock stability [46].

Two degrees of freedom of the microcomb are stabilized using passive and active optical clocks. Alternatively, one may re-design the microcavity II to reduce the FSR down to tens of GHz. Thus, the mode spacing f_{rep} can be directly measured using a fast photodiode and the pump

power launched into the microcavity II is controlled accordingly. In this case, the active clock is separated from the stabilization loop of the microcomb, allowing for performing the frequency comparison between two optical clocks with distinct (i.e., passive vs. active) operation modes through the microcomb.

Funding. National Time Service Center (E239SC11); Engineering and Physical Sciences Research Council (EP/R031428/1); European Research Council ("CounterLight", 756966); Marie Skłodowska Curie Innovative Training Network ("Microcombs" 812818).

Disclosures. The authors declare no conflicts of interest.

Data availability. Data underlying the results presented in this paper are not publicly available at this time but may be obtained from the authors upon reasonable request.

Supplemental document. See [Supplement 1](#) for supporting content.

References

1. J. Ye, H. J. Kimble, and H. Katori, "Quantum state engineering and precision metrology using state-insensitive light traps," *Science* **320**(5884), 1734–1738 (2008).
2. H. Katori, "Optical lattice clocks and quantum metrology," *Nat. Photonics* **5**(4), 203–210 (2011).
3. E. Oelker, R. B. Hutson, C. J. Kennedy, L. Sonderhouse, T. Bothwell, A. Goban, D. Kedar, C. Sanner, J. M. Robinson, G. E. Marti, D. G. Matei, T. Legero, M. Giunta, R. Holzwarth, F. Riehle, U. Sterr, and J. Ye, "Demonstration of 4.8×10^{-17} stability at 1 s for two independent optical clocks," *Nat. Photonics* **13**(10), 714–719 (2019).
4. T. Bothwell, D. Kedar, E. Oelker, J. M. Robinson, S. L. Bromley, W. L. Tew, J. Ye, and C. J. Kennedy, "JILA SrI optical lattice clock with uncertainty of 2.0×10^{-18} ," *Metrologia* **56**(6), 065004 (2019).
5. R. Wynands and S. Weyers, "Atomic fountain clocks," *Metrologia* **42**(3), S64–S79 (2005).
6. A. Derevianko and H. Katori, "Colloquium: Physics of optical lattice clocks," *Rev. Mod. Phys.* **83**(2), 331–347 (2011).
7. J. Chen, "Active optical clock," *Chin. Sci. Bull.* **54**(3), 348–352 (2009).
8. M. A. Norcia, J. R. K. Cline, J. A. Muniz, J. M. Robinson, R. B. Hutson, A. Goban, G. E. Marti, J. Ye, and J. K. Thompson, "Frequency measurements of superradiance from the strontium clock transition," *Phys. Rev. X* **8**(2), 021036 (2018).
9. D. J. Jones, S. Diddams, A. Stentz, R. S. Windeler, J. L. Hall, and S. T. Cundiff, "Carrier-envelope phase control of femtosecond mode-locked lasers and direct optical frequency synthesis," *Science* **288**(5466), 635–639 (2000).
10. T. Schuldt, M. Gohlke, M. Oswald, J. Wüst, T. Blomberg, K. Döringshoff, A. Bawamia, A. Wicht, M. Lezius, K. Voss, M. Krutzik, S. Herrmann, E. Kovalchuk, A. Peters, and C. Braxmaier, "Optical clock technologies for global navigation satellite systems," *GPS Solut.* **25**(3), 83 (2021).
11. V. S. Ilchenko, A. A. Savchenkov, A. B. Matsko, and L. Maleki, "Nonlinear optics and crystalline whispering gallery mode cavities," *Phys. Rev. Lett.* **92**(4), 043903 (2004).
12. T. Carmon and K. J. Vahala, "Visible continuous emission from a silica microphotonic device by third-harmonic generation," *Nat. Phys.* **3**(6), 430–435 (2007).
13. J. U. Fürst, D. V. Strekalov, D. Elser, M. Lassen, U. L. Andersen, C. Marquardt, and G. Leuchs, "Naturally phase-matched second-harmonic generation in a whispering-gallery-mode resonator," *Phys. Rev. Lett.* **104**(15), 153901 (2010).
14. M. Yu, Y. Okawachi, C. Joshi, X. Ji, M. Lipson, and A. L. Gaeta, "Gas-phase microresonator-based comb spectroscopy without an external pump laser," *ACS Photonics* **5**(7), 2780–2785 (2018).
15. H. Shu, L. Chang, Y. Tao, B. Shen, W. Xie, M. Jin, A. Nethererton, Z. Tao, X. Zhang, R. Chen, B. Bai, J. Qin, S. Yu, X. Wang, and J. E. Bowers, "Microcomb-driven silicon photonic systems," *Nature* **605**(7910), 457–463 (2022).
16. Z. L. Newman, V. Maurice, and T. Drake, *et al.*, "Architecture for the photonic integration of an optical atomic clock," *Optica* **6**(5), 680–685 (2019).
17. S. B. Papp, K. M. Beha, P. P. Del'Haye, F. J. Quinlan, H. Lee, K. J. Vahala, and S. A. Diddams, "Microresonator frequency comb optical clock," *Optica* **1**(1), 10–14 (2014).
18. P. Del'Haye, A. C. Coillet, T. M. Fortier, K. M. Beha, D. C. Cole, H. Lee, K. J. Vahala, S. B. Papp, and S. A. Diddams, "Phase-coherent microwave-to-optical link with a self-referenced microcomb," *Nat. Photonics* **10**(8), 516–520 (2016).
19. H. Jung, R. Stoll, X. Guo, D. Fischer, and H. X. Tang, "Green, red, and IR frequency comb line generation from single IR pump in AlN microring resonator," *Optica* **1**(6), 396–399 (2014).
20. S. H. Lee, D. Y. Oh, Q.-F. Yang, B. Shen, H. Wang, K. Y. Yang, Y.-H. Lai, X. Yi, X. Li, and K. Vahala, "Towards visible soliton microcomb generation," *Nat. Commun.* **8**(1), 1295 (2017).
21. P. Del'Haye, O. Arcizet, A. Schliesser, R. Holzwarth, and T. J. Kippenberg, "Full stabilization of a microresonator-based optical frequency comb," *Phys. Rev. Lett.* **101**(5), 053903 (2008).
22. O. S. Heavens, "Radiative transition probabilities of the lower excited states of the alkali metals," *J. Opt. Soc. Am.* **51**(10), 1058–1061 (1961).
23. F. Vollmer and D. Yu, *Optical Whispering Gallery Modes for Biosensing: From Physical Principles to Applications* (Springer International Publishing, 2020) pp. 194–197.

24. U. Gubler and C. Bosshard, "Optical third-harmonic generation of fused silica in gas atmosphere: Absolute value of the third-order nonlinear optical susceptibility $\chi^{(3)}$," *Phys. Rev. B* **61**(16), 10702–10710 (2000).
25. C. Ming, O. Oskar, and K. J. Vahala, "Observation of critical coupling in a fiber taper to a silica-microsphere whispering-gallery mode system," *Phys. Rev. Lett.* **85**(1), 74–77 (2000).
26. D. Yu and F. Vollmer, "Allan deviation tells the binding properties in single-molecule sensing with whispering-gallery-mode optical microcavities," *Phys. Rev. Res.* **3**(2), 023087 (2021).
27. D. Yu, L. C. Kwek, L. Amico, and R. Dumke, "Theoretical description of a micromaser in the ultrastrong-coupling regime," *Phys. Rev. A* **95**(5), 053811 (2017).
28. D. Yu and R. Dumke, "Open Ising model perturbed by classical colored noise," *Phys. Rev. A* **100**(2), 022124 (2019).
29. D. Yu and F. Vollmer, "Spontaneous PT-symmetry breaking in lasing dynamics," *Commun. Phys.* **4**(1), 77 (2021).
30. D. Yu and F. Vollmer, "Active optomechanics," *Commun. Phys.* **5**(1), 61 (2022).
31. K. W. Martin, G. Phelps, N. D. Lemke, M. S. Bigelow, B. Stuhl, M. Wojcik, M. Holt, I. Coddington, M. W. Bishop, and J. H. Burke, "Compact optical atomic clock based on a two-photon transition in rubidium," *Phys. Rev. Appl.* **9**(1), 014019 (2018).
32. H. Stoehr, F. Mensing, J. Helmcke, and U. Sterr, "Diode laser with 1 Hz linewidth," *Opt. Lett.* **31**(6), 736–738 (2006).
33. S. J. M. Kuppens, M. P. van Exter, and J. P. Woerdman, "Quantum-limited linewidth of a bad-cavity laser," *Phys. Rev. Lett.* **72**(24), 3815–3818 (1994).
34. M. I. Kolobov, L. Davidovich, E. Giacobino, and C. Fabre, "Role of pumping statistics and dynamics of atomic polarization in quantum fluctuations of laser sources," *Phys. Rev. A* **47**(2), 1431–1446 (1993).
35. K. S. Kim, R. H. Stolen, W. A. Reed, and K. W. Quoi, "Measurement of the nonlinear index of silica-core and dispersion-shifted fibers," *Opt. Lett.* **19**(4), 257–259 (1994).
36. P. Del'Haye, T. Herr, E. Gavartin, M. L. Gorodetsky, R. Holzwarth, and T. J. Kippenberg, "Octave spanning tunable frequency comb from a microresonator," *Phys. Rev. Lett.* **107**(6), 063901 (2011).
37. T. J. Kippenberg, S. M. Spillane, and K. J. Vahala, "Kerr-nonlinearity optical parametric oscillation in an ultrahigh-Q toroid microcavity," *Phys. Rev. Lett.* **93**(8), 083904 (2004).
38. P. Del'Haye, A. Schliesser, O. Arcizet, T. Wilken, R. Holzwarth, and T. J. Kippenberg, "Optical frequency comb generation from a monolithic microresonator," *Nature* **450**(7173), 1214–1217 (2007).
39. Y. K. Chembo and C. R. Menyuk, "Spatiotemporal Lugiato-Lefever formalism for Kerr-comb generation in whispering-gallery-mode resonators," *Phys. Rev. A* **87**(5), 053852 (2013).
40. I. H. Malitson, "Interspecimen comparison of the refractive index of fused silica," *J. Opt. Soc. Am.* **55**(10), 1205–1208 (1965).
41. C. Z. Tan and J. Arndt, "Temperature dependence of refractive index of glassy SiO₂ in the infrared wavelength range," *J. Phys. Chem. Solids* **61**(8), 1315–1320 (2000).
42. X. Sun, R. Luo, X.-C. Zhang, and Q. Lin, "Squeezing the fundamental temperature fluctuations of a high-Q microresonator," *Phys. Rev. A* **95**(2), 023822 (2017).
43. J. Miao, T. Shi, J. Zhang, and J. Chen, "Compact 459-nm Cs cell optical frequency standard with $2.1 \times 10^{-13} / \sqrt{\tau}$ short-term stability," *Phys. Rev. Appl.* **18**(2), 024034 (2022).
44. P. Chang, S. Zhang, H. Shang, and J. Chen, "The lasing realization of Rb four-level active optical clock," *IEEE International Frequency Control Symposium* **2018** 1–4 (2018).
45. T. Shi, D. Pan, and J. Chen, "Realization of phase locking in good-bad-cavity active optical clock," *Opt. Express* **27**(16), 22040–22052 (2019).
46. T. Shi, D. Pan, W. Zhuang, X. Guan, J. Miao, J. Zhang, and J. Chen, "Active optical clock based on laser cooling of alkali-metal atoms," *Joint Conference of the European Frequency and Time Forum and IEEE International Frequency Control Symposium* **2021** 1–3 (2021).